

# Proven Tissue Equivalent Phantom Solutions

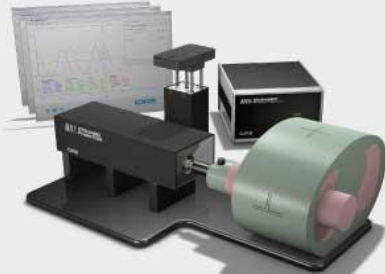


High fidelity simulation for your SRS program

CIRS is recognized as a leader in the manufacturer of tissue equivalent phantoms for medical imaging, radiation therapy and procedural training.

CIRS is one of a few companies worldwide with proprietary technology that permits the manufacture of phantoms for every commercial imaging modality.

*Visit Us at RSNA, Booth 2700*



Programmable motion for image acquisition, treatment planning & dose delivery



Our most realistic maxillofacial phantom for dental cone beam CT & panoramic X-Ray



Measure known kPa's with shear wave systems



MR, CT & Ultrasound compatible



Required for MQSA Program



Evaluate FFDM system performance



Most complete solution for performance and QA testing

## CIRS

900 Asbury Ave. • Norfolk, Virginia 23513 • USA • Tel: 757-855-2765 • [WWW.CIRSINC.COM](http://WWW.CIRSINC.COM)

# Thresholds for detecting and characterizing focal lesions using steady-state MR elastography

Marvin M. Doyley<sup>a)</sup> and John B. Weaver

*Department of Radiology, Dartmouth-Hitchcock Medical Center, Lebanon, New Hampshire 03756  
and Thayer School of Engineering, Dartmouth College, Hanover, New Hampshire 03755*

Elijah E. W. Van Houten and Francis E. Kennedy

*Thayer School of Engineering, Dartmouth College, Hanover, New Hampshire 03755*

Keith D. Paulsen

*Thayer School of Engineering, Dartmouth College, Hanover, New Hampshire 03755  
and Norris Cotton Cancer Center, Lebanon, New Hampshire 03756*

(Received 7 August 2002; accepted for publication 8 January 2003; published 17 March 2003)

An objective contrast-detail analysis was performed in this study to assess the low contrast detectability of a clinical prototype harmonic magnetic resonance elastographic imaging system. Elastographic imaging was performed on gelatin phantoms containing spherical inclusions of varying size and modulus contrast. The results demonstrate that lesions as small as 5 mm can be detected with a minimum modulus contrast of 14 dB. However, the shear modulus of such small lesions was not accurately recovered. In general, the shear modulus of larger focal lesions was accurately (i.e., within 25% of the true value) recovered. The minimum modulus contrast needed to detect focal lesions was observed to decrease with increasing lesion size. © 2003 American Association of Physicists in Medicine. [DOI: 10.1118/1.1556607]

**Key words:** Breast cancer detection, contrast-detail analysis, elastography, elasticity imaging, magnetic resonance imaging, performance characterization

## I. INTRODUCTION

Pathological abnormalities such as breast tumors are often accompanied by changes in tissue elasticity.<sup>1</sup> This forms the basis of manual palpation, which is routinely used for the subjective clinical assessment of tissue elasticity. The shear modulus of breast tumors can be as much as an order of magnitude higher than normal breast tissues.<sup>2,3</sup> Nevertheless, early malignancies can elude detection by manual palpation by virtue of their size and/or location within the breast. This limitation can be overcome using a system that is capable of imaging tissue elasticity. Unfortunately, none of the established medical imaging modalities, such as magnetic resonance imaging (MRI), ultrasonography (US), or x-ray computed tomography (CT), can provide a direct measure of tissue elasticity; however, most can provide information regarding induced tissue motion, which is related to tissue elasticity.

Several ultrasonic methods for imaging tissue elasticity have appeared in the literature;<sup>4–8</sup> a detailed review of these techniques is given in Ophir *et al.*,<sup>9</sup> Gao *et al.*,<sup>10</sup> Parker *et al.*,<sup>11</sup> and Bamber *et al.*<sup>12</sup> The clinical results produced with these approaches have been very encouraging.<sup>13–16</sup> However, ultrasonic elastography may not be suited for clinical applications that require accurate quantification of tissue elastic properties. Potential clinical applications include monitoring tumor response to therapy and differentiating between tissue types for disease detection. The accurate quantification of tissue elasticity requires measurement of all components of the induced internal displacements. Unfortunately, current ultrasonic displacement estimation methods

are limited by poor resolution in the off-axial direction inherent to ultrasound imaging.

Magnetic resonance imaging, although more expensive than diagnostic ultrasound, has several distinct advantages, which makes it more suited for quantitative elastography. For instance, all components of the induced internal tissue displacements can be measured with high precision using MRI. Furthermore, the displacement sensitivity of magnetic resonance imaging is superior to ultrasonography, which makes it appealing when measuring small (micron scale) internal tissue displacements. Consequently, various groups<sup>17–27</sup> including our own<sup>28–30</sup> are actively developing magnetic resonance (MR) based elastographic imaging techniques.

The long-term objective of this work is to improve the differential diagnosis of breast cancer by developing a clinically useful MR elastographic imaging system. Therefore, objective criterion must be defined for assessing and optimizing all stages of the elastographic image formation process illustrated in Fig. 1.

The ability to detect low contrast focal lesions is an important attribute of any medical imaging system. The established framework of a contrast-detailed analysis is generally used to assess the low contrast detectability of medical imaging system.<sup>31–35</sup> This is generally performed subjectively by conducting several psychophysical experiments with human observers, where the goal is to detect lesions that lie on the threshold of detectability by virtue of their size and contrast.<sup>33,36</sup> Consequently, the repeatability of most contrast-detail analysis is generally poor. An objective

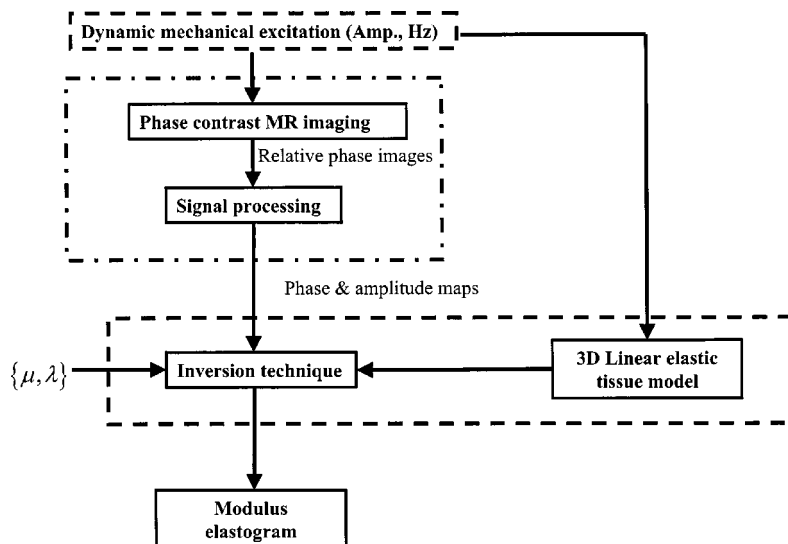


FIG. 1. Flow chart describing the three-step process used to generate a harmonic elastogram. First, the tissue under investigation is stimulated mechanically using a deformation device. Second, the amplitude and phase of the induced tissue motion is measured by processing relative phase images, which are acquired using a phase contrast MR imaging sequence. Third, the spatial distribution of the shear modulus distribution is estimated by applying a model-based inversion technique to MR measured motion images.

contrast-detail analysis based on the match-filter concept<sup>37,38</sup> was employed in this study to determine the minimum modulus contrast required for both detecting and characterizing focal lesions using a clinical prototype magnetic resonance elastographic imaging system.<sup>28</sup>

## II. MATERIALS AND METHODS

### A. Phantoms

Four groups of elasticity phantoms containing spherical inclusions, which had diameters of 5, 10, 18, and 25 mm, were manufactured in a repeatable and controlled manner from porcine skin gelatin (Type A, approximately 175 bloom, Sigma Chemical Co., St. Louis, MO), formaldehyde (Sigma Chemical Co., St. Louis, MO), distilled water (18 MΩ), and ethylenediamine tetra-acetic acid (Sigma Chemical Co., St. Louis, MO). Each group contained six phantoms with similar size spherical inclusions but different modulus contrast. [Modulus contrast is defined (in dB) as  $20 \log_{10}(\mu_L/\mu_B)$ , where  $\mu_L$  and  $\mu_B$  represent the shear modulus in the inclusion and background, respectively.] Modulus contrast of the phantoms was varied from 3 dB (1:1.4) to 17 dB (1:7) by changing the ratio of gelatin concentration used to fabricate the inclusion relative to that used to construct the background material. The general com-

position of the materials employed is given in Table I. Copper sulphate (1.29 mg/ml) was added to all lesions to allow their position and extent to be identified in the magnitude MR images. Lesions with identical diameters were manufactured using one of four molds. Each mold consisted of two acrylic blocks with aligned hemispherical depressions. Figure 2 shows representative examples of simulated lesions that were manufactured. All phantoms produced in this study were assembled as follows. First, a relatively thin layer (i.e., 10 mm thick) of background material was set evenly in the bottom of a 4.7 cm<sup>3</sup> Plexiglas mould. Next, the simulated lesion was placed approximately in the center of the gelatin layer and carefully covered with cooled ( $\approx 24^\circ\text{C}$ ) but still liquid background material. The resulting phantom was sealed to minimize dehydration, and stored at  $4^\circ\text{C}$  for approximately 24 h to stabilize the mechanical properties before imaging, as recommended by de Korte et al.<sup>39</sup>

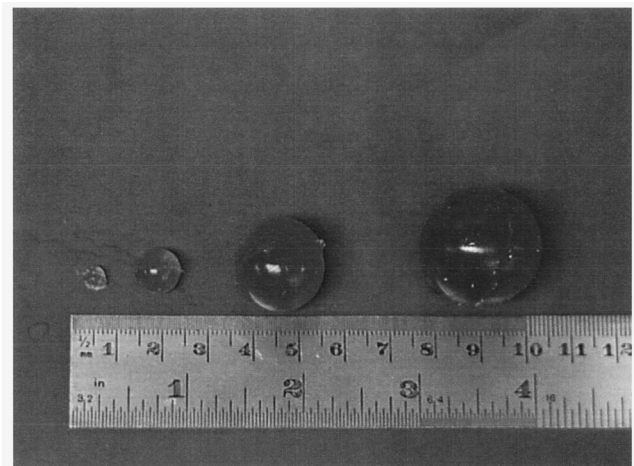


FIG. 2. Photograph showing an example of spherical gelatin inclusions used to simulate focal lesions. The green colorization is due to the presence of copper sulphate, which was used as a contrast agent to allow the position and extent of the inclusion to be discernible in the MR magnitude images.

TABLE I. Concentration in percentage by weight of materials used to construct contrast-detail phantoms.

Material	Gelatin	Formaldehyde (0.2% conc.)	Distilled water	EDTA
Background	6	10	82	2
Sphere # 1	8	10	80	2
Sphere # 2	10	10	78	2
Sphere # 3	14	10	74	2
Sphere # 4	18	10	70	2
Sphere # 5	20	10	68	2
Sphere # 6	25	10	63	2



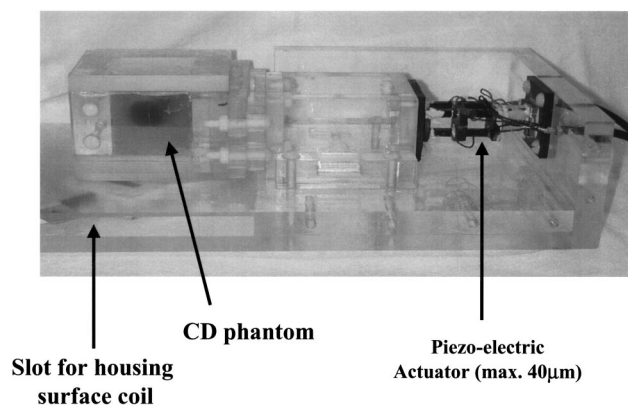


FIG. 3. A photograph of the MR compatible dynamic mechanical deformation device, which was used to induce steady-state time-harmonic displacements within the phantoms under investigation.

## B. Mechanical excitation and motion estimation

Each phantom was warmed to room temperature and mounted in our MR compatible dynamic mechanical deformation device, as illustrated in Fig. 3. The data was acquired and processed, as previously described.<sup>28</sup> The piezoelectric actuator was driven to its maximum displacement of 40  $\mu\text{m}$  at 100 Hz using a sinusoidal voltage produced using a signal generator (Model HP33120A). The internal clock of the signal generator was phased locked with a 10 MHz MR system clock to eliminate phase jitter during data acquisition. All MR imaging was performed with a five-inch surface coil, which was mounted in a slot below the phantom, on a 1.5 T whole body imager (GE Medical Imaging Systems, Milwaukee WI). The phase and amplitude of the time-harmonic, steady-state displacement distribution were measured using a simple motion encoding pulse sequence. The scanner was configured to operate with an echo time (TE) of 15.6 ms, a repetition time (TR) of 20.6 ms, and a flip angle of 30°. Four relative phase images were acquired from each slice with a matrix resolution of 256 $\times$ 256 from a 16 cm<sup>2</sup> field of view (FOV), which were averaged in a phase-cycling mode to minimize baseline phase errors.

Twenty-six (3 mm thick) axial phase images were acquired in each coordinate direction from the phantoms containing 18 and 25 mm diameter lesions; whereas 32 (2 mm thick) and 60 (1 mm thick) phase images were acquired over the same FOV from the phantoms containing 10 and 5 mm diameter lesions, respectively.

All axial phase images were transferred from the MR imager and stored on a 1 GHz Pentium III workstation (Dell precision, model 420) where the phase and amplitude of the displacement field were estimated by applying a pointwise least squares fitting procedure implemented in MATLAB<sup>TM</sup>.

## C. Shear modulus estimation

The spatial variation in shear modulus was computed using a three-dimensional (3-D) nodal-based subzone inversion technique<sup>29</sup> that use the finite element method and a modified Newton–Raphson iterative scheme. Finite element represen-

tations of the phantoms were produced using the technique described in Paulsen *et al.*<sup>40</sup> Boundary meshes, a prerequisite of this technique, were constructed by applying a marching cube algorithm<sup>41</sup> to MR magnitude images that had been manually segmented using the Analyze software package (Mayo Foundation, 1998). A typical three-dimensional finite element mesh used comprised of approximately 200 000 elements and 60 000 nodes.

The internal tissue displacements were interpolated to the nodes of all finite element meshes using MATLAB<sup>TM</sup> cubic interpolation function. The finite element meshes were divided into approximately 500 overlapping subzones, which contained 450 nodes spanning an average distance of 5 mm. The spatial distribution of Lamé elastic constants in each subzone was reconstructed using the assumption that the tissue under investigation was initially elastically homogeneous. For the purpose of this study, trial values of 2 kPa ( $\mu$ ) and 100 kPa ( $\lambda$ ) were used as the initial estimates. The reconstruction procedure to update the elastic constants of a typical subzone can be summarized into the following steps.

(1) Compute the displacement at each nodal point based on the current value of Lamé elastic constants by solving the partial differential equation governing the harmonic elasticity problem, which is given by

$$(\lambda + \mu)\nabla(\nabla \cdot u) + \mu \nabla^2 u = \rho \frac{\partial u^2}{\partial t^2}, \quad (1)$$

where  $u$  is the nodal displacement vector,  $\rho$  is the medium's density [assumed to be equivalent to the density of water ( $\approx 1 \text{ kg/m}^3$ )], and  $\nabla$  is the del operator.

(2) Compute the residual displacement vector,  $\{\Delta U\}$ , by subtracting the calculated displacements from the measured displacement at each subzone nodal point.

(3) Construct the Jacobian using the method described in Kallel and Bertrand.<sup>42</sup>

(4) Compute the updates to the trial solution  $\{\Delta\mu, \Delta\lambda\}$  by solving the normal equations describing the least-squares problem using Marquardt's approach,<sup>43</sup> i.e.,

$$[J^T J + I\alpha] \begin{Bmatrix} \Delta\mu \\ \Delta\lambda \end{Bmatrix} = -[J^T] \{\Delta U\}, \quad (2)$$

where the matrix on the left-hand side represents the Hessian, the matrix on the right-hand side represents the transposed Jacobian, and  $\alpha$  is the regularization parameter.

(5) Update the value of Lamé elastic constants at the next iteration based on the current solution for  $\{\Delta\mu, \Delta\lambda\}$  from Eq. (2).

(6) Repeat steps (1)–(5) multiple times (generally twice) until the root mean squared error between the measured and computed displacement is reduced, then randomly select another subzone.

The algorithm is said to have completed a global iteration when all subzones have been treated. In this study, all reconstructions were terminated after 35 global iterations. In our experience, the reconstruction procedure generally converges to a stable solution in 30–35 global iterations. Solving for  $\{\Delta\mu, \Delta\lambda\}$  using the Marquardt methods involves a

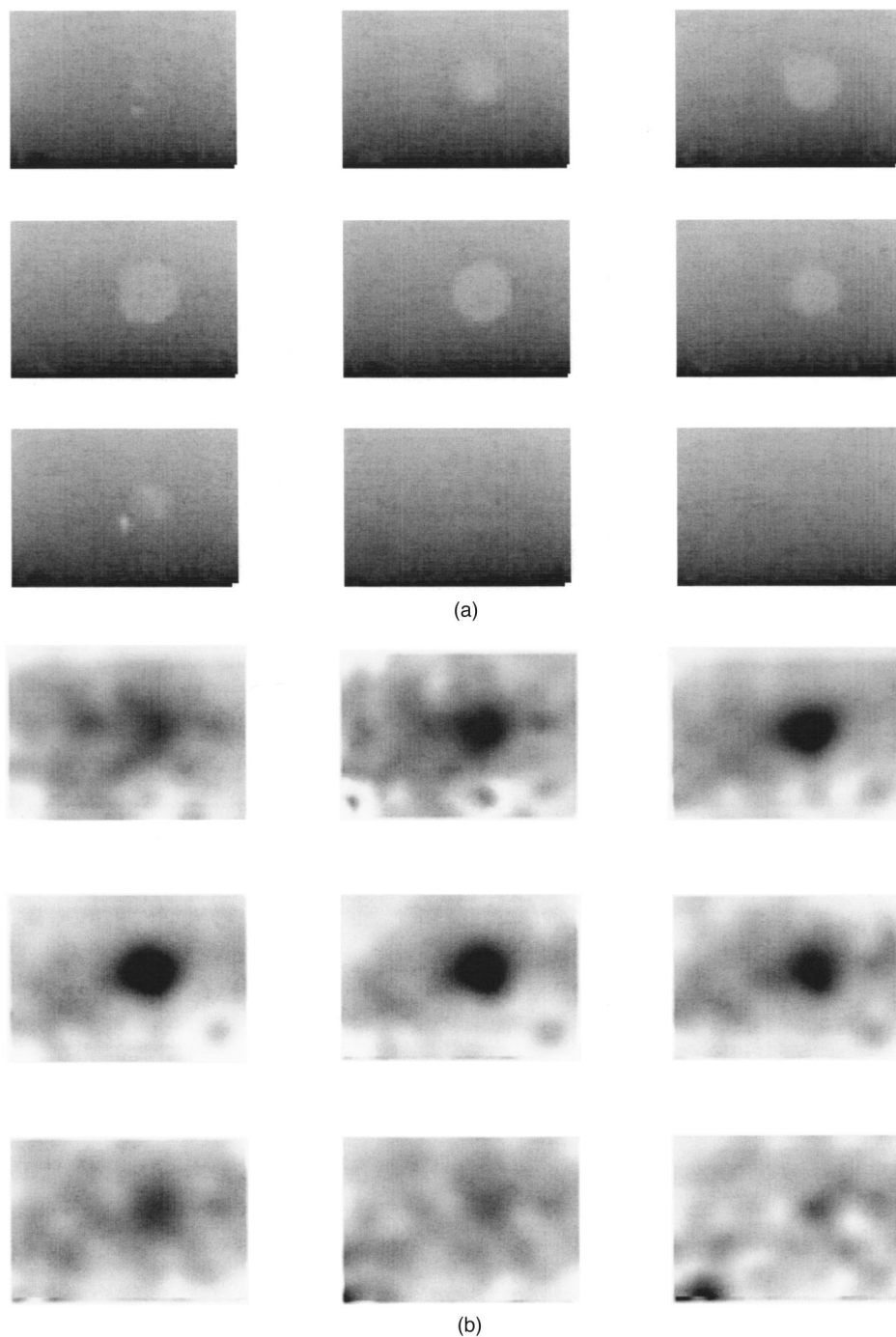


FIG. 4. Axial MR magnitude images (a) and corresponding elastograms (b) obtained from the center of 9 dB (3:1) modulus contrast phantom [3.5 cm (height)  $\times$  4.1 cm (width)  $\times$  16 mm FOV]. In all elastograms the 2–6 kPa shear modulus range is from black to white.

two-step procedure. First, both sides of Eq. (2) are scaled. Then a positive scalar (i.e., the regularization parameter, which was incidentally set to  $10^{-4}$  in all reconstructions) is added to the diagonal of the scaled Hessian. This forces the reconstruction technique to converge to a stable solution. Spatial filtering was performed at all global iterations to increase the stability of the inversion technique, particularly in the presence of measurement noise.<sup>44</sup> The linear filtering operation, which was performed at the  $(k+1)$ th global iteration, is given by

$$\begin{Bmatrix} \mu \\ \lambda \end{Bmatrix}_{k+1}^{\text{new}} = [F] \begin{Bmatrix} \mu \\ \lambda \end{Bmatrix}_{k+1}^{\text{old}}, \quad (3)$$

where  $[F]$  is the sparse filtering matrix computed at the start of all reconstructions. A more detailed description of the spatial filtering technique is given in Doyley *et al.*<sup>44</sup>

High-resolution shear modulus elastograms were generated by resampling the shear modulus estimates computed on the finite element mesh to the same FOV and voxel

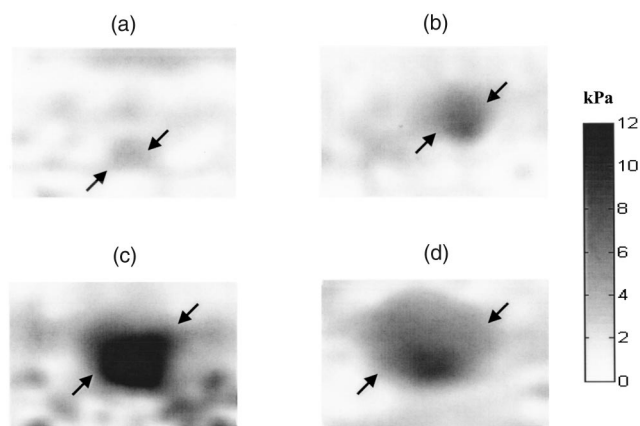


FIG. 5. Axial elastograms obtained from the central plane from a high modulus contrast (17 dB) elasticity phantoms containing (a) 5 mm, (b) 10 mm, (c) 18 mm, and (d) 25 mm diameter lesions and each image has a dimension of approximately 4 cm×5 cm.

resolution (0.64 mm×0.64 mm×slice thickness, i.e., 1, 2, or 3 mm, depending on size of the containing lesion) as the MR phase images.

#### D. Assessing lesion detectability and characterization

Lesion detectability was assessed objectively using the match filter concept, which is sometimes referred to as the

contrast observer.<sup>38,39</sup> The basic premise of this technique is that the likelihood of detecting a lesion can be expressed in the form of contrast-to-noise ratio (CNR), which in elastography is defined as<sup>45,46</sup>

$$\text{CNR} = \sqrt{\frac{2(\hat{\mu}_L - \hat{\mu}_B)^2}{\sigma_L^2 + \sigma_B^2}} \quad (4)$$

where  $\hat{\mu}_L$  and  $\hat{\mu}_B$  represent the mean shear modulus computed over similar size regions in the lesion and background tissue, respectively; whereas  $\sigma_L^2$  and  $\sigma_B^2$  represent the variance of shear modulus in their respective volume. The noise in modulus elastograms is spatially dependent due to the nonlinear nature of the inverse reconstruction procedure; consequently  $\hat{\mu}_B$  and  $\sigma_B^2$  were computed over the entire background. The object was perceived as being detected if the CNR was greater than or equal to 2.2. This decision criterion was selected based on the recommendation of an experienced observer. It is important to note that the experienced observer threshold is based on having knowledge of lesion position.

Accuracy was assessed by comparing the mean shear modulus recovered over the inclusion relative to independent estimates of shear modulus, which were measured, as described in Appendix A. The reconstructed object was considered accurately characterized if the mean shear modulus computed in the lesion was within 25% of the true value.

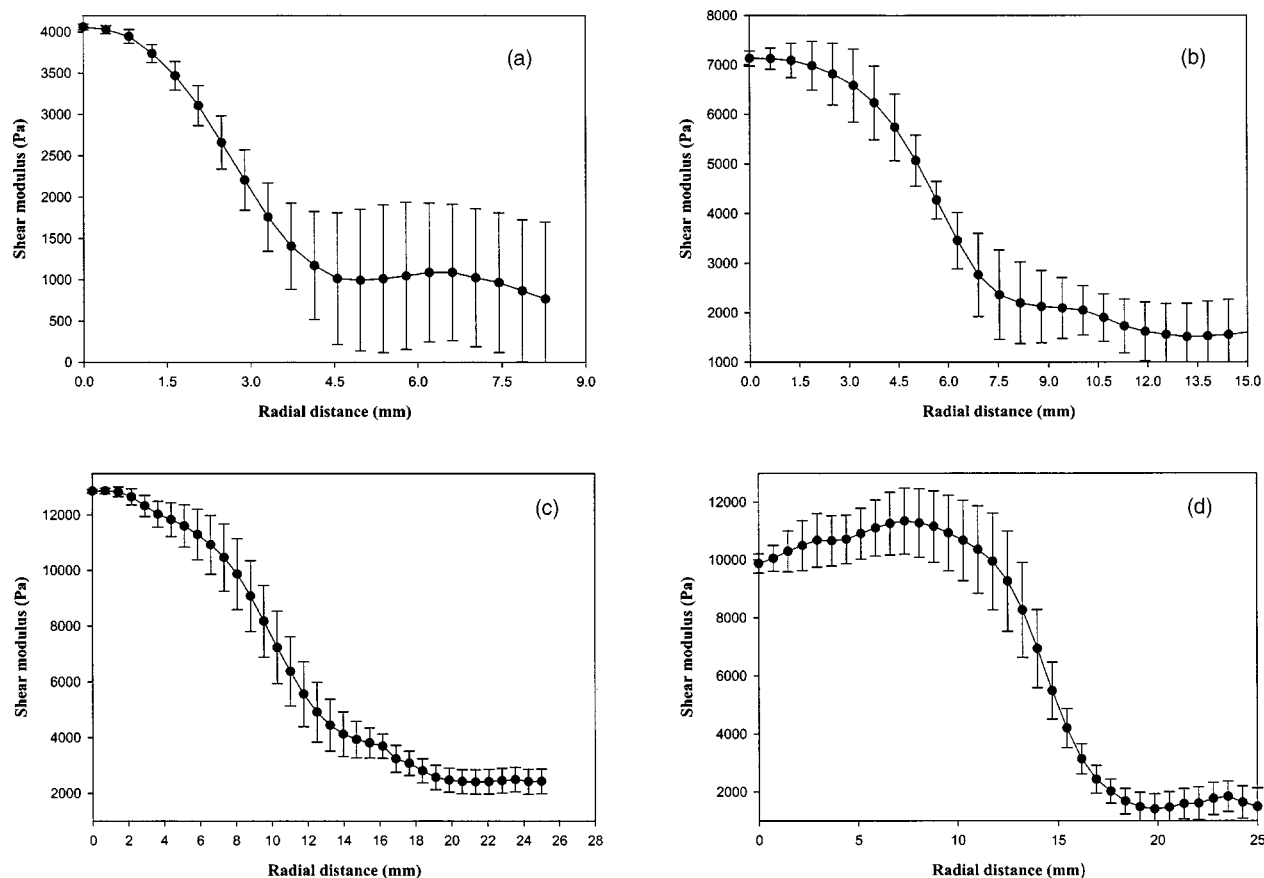


FIG. 6. Mean radial profiles computed from the elastograms shown in Fig. 5. The error bars represent  $\pm$  one standard deviation over 15 radial profiles through the center of the inclusion.

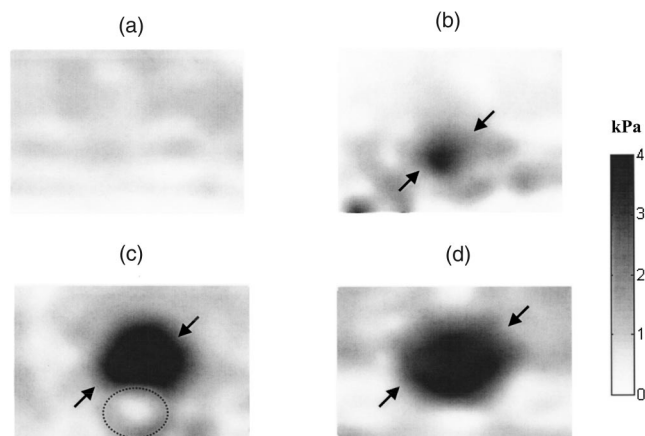


FIG. 7. Axial elastograms obtained from the central plane of low modulus contrast (6 dB) elasticity phantoms containing (a) 5 mm, (b) 10 mm, (c) 18 mm, and (d) 25 mm diameter lesions. Arrows indicate either the position of the lesion or artifacts due to the presence of gas bubbles. Each image has a dimension of approximately 4 cm $\times$ 5 cm.

This decision criterion represents the maximum error incurred between the shear modulus recovered for an elastically homogeneous phantom and the shear modulus measured using the mechanical analyzer.

### III. RESULTS

Figure 4 shows examples of MR magnitude images [Fig. 4(a)] and modulus elastograms [Fig. 4(b)] obtained from a phantom containing a 10 mm diameter inclusion, which was approximately three times stiffer than the background. The inclusion's position and extent can clearly be visualized in both sets of images, which demonstrates that elastography is able to provide information that is generally not present in conventional MR data.

Figure 5 shows examples of elastograms obtained from the central plane from high modulus contrast (17 dB) phantoms containing lesions with varying diameters. A focal inclusion as small as 5 mm in diameter can be visualized at this modulus contrast, which would represent a significant improvement over the smallest deep-seated focal lesion that can clinically be detected in the breast using manual palpation. However, large bias was incurred when estimating the shear modulus of lesions that were  $<18$  mm in diameter. Figure 6 shows the mean of 15 radial profiles passing through the center of each elastogram presented in Fig. 5, equally distributed between  $0^\circ$  and  $360^\circ$ . The center and radius of the lesion was determined by fitting a circle to a contour enclosing the inclusion. Note that the spatial filter rather than the lesion dominates the shape of the radial profiles causing the inclusions in the elastograms to appear consistently larger than their actual size. Interestingly, better precision (i.e., smaller variance) in the shear modulus estimate was obtained in the inclusion relative to the background for the phantom containing the 5 mm diameter object [Fig. 6(a)]; whereas the shear modulus precision was more comparable in the inclusion and background for phantoms containing the larger heterogeneities [Figs. 6(b)–6(c)]. The precision in the

shear modulus estimated for the inclusion was inferior compared to that measured in the background for the 25 mm diameter inclusion [Fig. 6(d)]. This was due to the fact that the inclusion was unintentionally produced with a shear modulus gradient, which is clearly visible in the elastogram shown in Fig. 5(d). Figure 7 shows examples of elastograms obtained from the central plane of low contrast phantoms (6 dB) containing lesions of varying sizes. Note that the 5 mm diameter lesion was not discernible at this modulus contrast. It is interesting to note that the manufacturing defect observed in phantom containing the large inclusion [i.e., Fig. 5(d)] is not present.

Figure 8 shows scatter plots of the contrast-to-noise ratio [Fig. 8(a)] and the absolute error in shear modulus [Fig. 8(b)] of lesions that were perceived as being detected, and whose shear modulus was reconstructed within 25% of the true value. Note that although the prototype system was able to detect lesions as small as 5 mm in diameter, it was unable to accurately recover the shear modulus at this lesion size. Figure 9 shows plots of the minimum modulus contrast required to detect and accurately reconstruct the shear modulus of focal lesions as a function of lesion size.

### IV. DISCUSSION

In this paper we report the results of an objective contrast-detail analysis, which was conducted to determine the threshold modulus contrast required to detect and characterize focal lesions in elastograms produced by a clinical prototype harmonic elastographic imaging system.

Figure 9 demonstrates that the threshold modulus contrast needed to detect a focal lesion decreases with increasing lesion size, which is consistent with the observations of Miller and Bamber,<sup>47</sup> who performed psychophysical experiments using simulated sonograms with human observers. It is important to realize that in practical terms lesion detectability is basically a signal-to-noise ratio (SNR) problem. With this view in mind we would expect to detect 5 mm inclusions at lower modulus contrast by either decreasing the measurement noise and/or increasing the elastographic signal. The noise in the modulus elastograms is very complex, depending on several variables such as (a) the quality of the displacement estimates, which, in turn, will be determined primarily by the MR image noise, (b) the amplitude of the displacement field, and (c) those associated with the reconstruction procedure, such as the number of iterations, spatial filtering weight, regularization parameter, and the initial property distribution estimate. We are currently studying the individual and combine effects of the MR imaging parameters and reconstruction variables on reconstruction noise. The results of this investigation will be the focus of a future report.

It is apparent from Fig. 6 that excessive spatial filtering blurs the elastograms. This will reduce spatial resolution, and compromise our ability to accurately characterize tumor



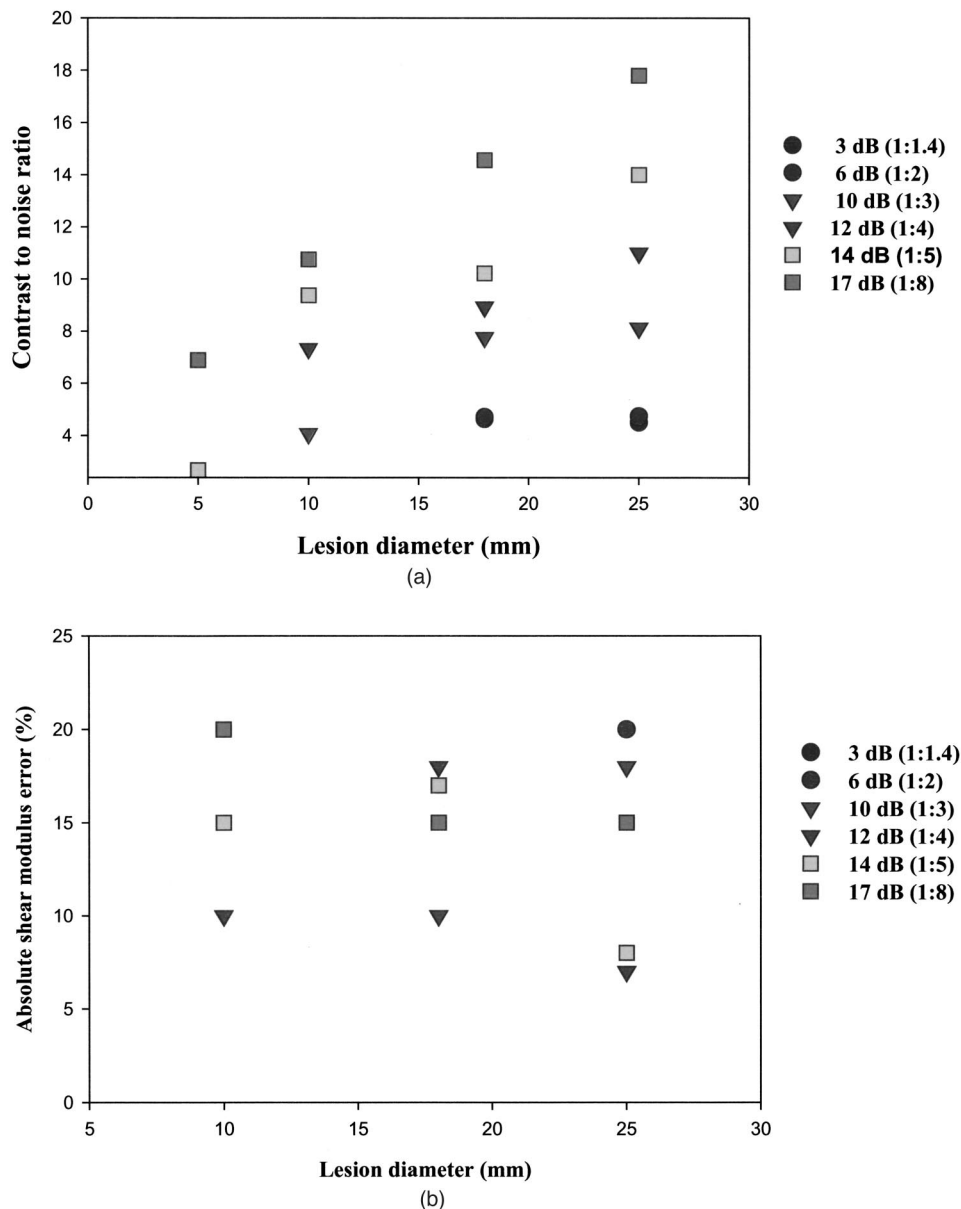


FIG. 8. Scatter plots of contrast-to-noise ratio for detected lesions (a), and absolute shear modulus error for accurately reconstructed lesions (b).

size using elastography. One solution to this problem would be to improve the quality of the MR displacement estimates by increasing the imaging time. This would allow us to perform less spatial filtering when reconstructing tissue elasticity.

It should also be noted that the inclusions generated in this study will have a tendency to swell because of the osmotic pressure gradient<sup>48,49</sup> generated by differences in gelatin concentration. In future studies, we plan to characterize the rate of swelling of the gelatin inclusions in order to quantify the extent of this effect.

A limitation in the current study is that we did not investigate the behavior of the reconstruction field with multiple inclusions, or to evaluate whether the contrast-to-noise ratio and accuracy of the reconstructed lesion is affected by the position in the imaging field of view. Further work

is currently planned to explore these parameters that impact the performance of the MRE imaging scheme.

## V. CONCLUSIONS

We have demonstrated using the framework of contrast-detail analysis that our clinical prototype steady-state magnetic resonance elastography system can detect lesions as small as 5 mm with a minimum modulus contrast of 14 dB. However, at the present time we are unable to accurately recover the elastic properties of an inclusion this small. It was shown that the minimum modulus contrast needed to visualize focal lesions decreases with increasing lesion size; results that are consistent with previously reported observa-



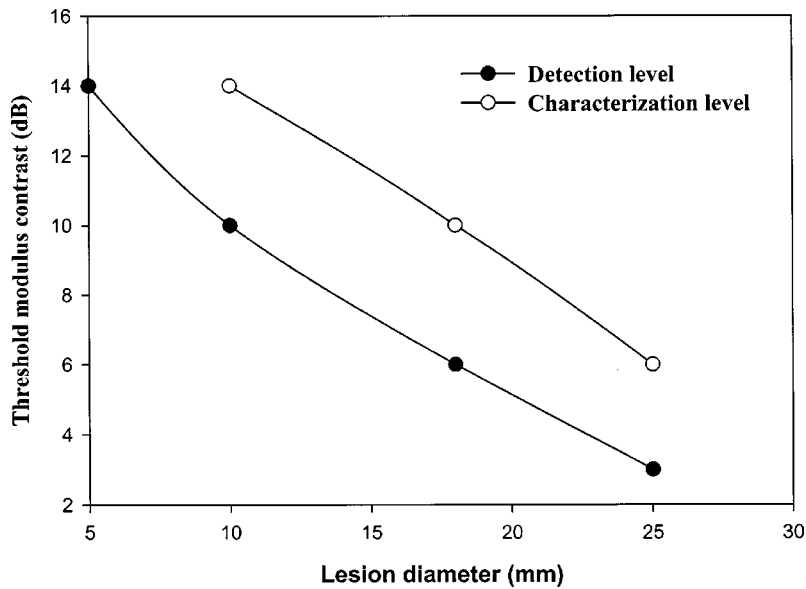


FIG. 9. Contrast-detail curve generated from scatter plots shown in Fig. 8.

tions. These results are sufficiently encouraging to warrant further development and evaluation with more complex models.

#### ACKNOWLEDGMENT

This work was funded by the National Cancer Institute Program Project Grant No. PO1-CA80139.

#### APPENDIX

The shear modulus of the simulated lesions and background phantom materials was measured at room temperature (22 °C) using the dynamic mechanical analyzer (AR 1000 ETC) shown in Fig. 10. All measurements were performed on elastically homogeneous cylindrically shaped samples (40 mm diameter×5 mm height) in collaboration with TA instruments (Newcastle, Delaware). The complex modulus of all samples was measured in a controlled strain



FIG. 10. Photograph of dynamic mechanical analyzer that was used to calibrate the shear modulus of contrast-detail phantoms.

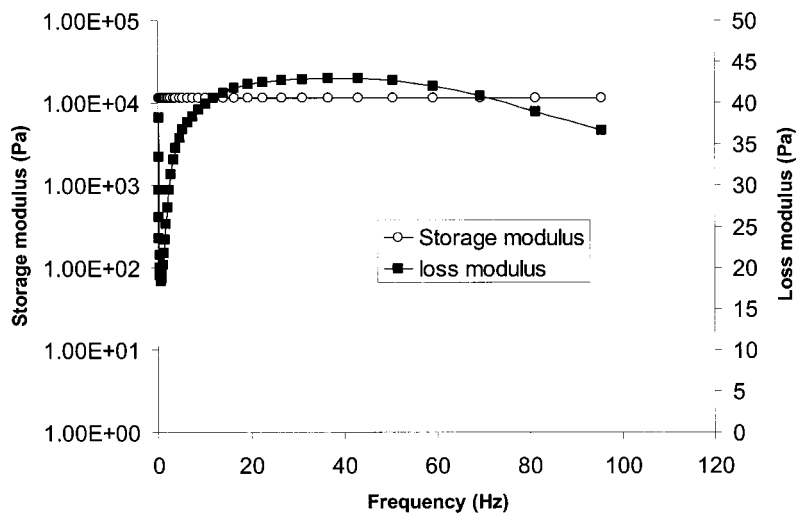


FIG. 11. The complex modulus of a 25% by weight gelatin sample, showing the variation of the storage ( $G'$ ) and loss ( $G''$ ) modulus with frequency.

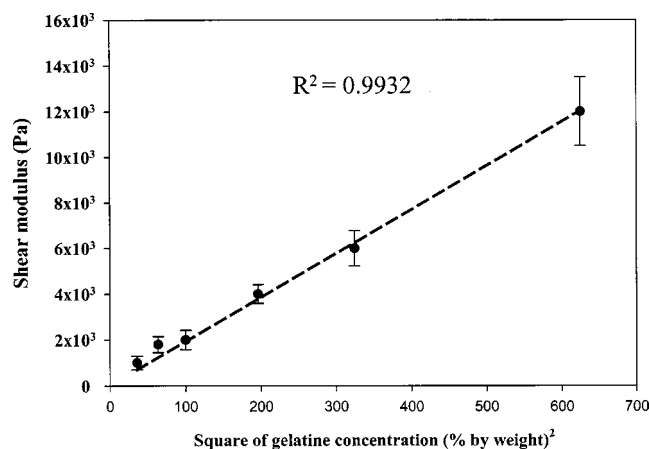


FIG. 12. Calibration curve used to assess the accuracy of the reconstructed elastograms.

mode (i.e., applying a sinusoidal oscillating strain, which had a peak-to-peak value of 0.05%, as determined from a constant strain mode experiment) with increasing frequency of vibration.

Figure 11 shows the complex modulus, which was obtained from a 6% by weight gelatin sample, plotted as a function of the frequency of excitation. At low frequencies (i.e.,  $\leq 100$  Hz) the storage modulus ( $G'$ ) is independent of frequency, whereas the loss modulus ( $G''$ ) is highly frequency dependent. This behavior is representative of that observed for all samples produced in this study, which suggests that at low frequencies, attenuation and other viscous effects are negligible. Figure 12 shows a plot of the mean shear modulus  $\pm$  one standard deviation, which was measured from five different samples plotted as a function of the square of gelatin concentration. This figure was used as the basis for assessing the accuracy of the reconstructed images. Note that this curve confirms previously reported observations that for low gelatin concentration (i.e.,  $\leq 25\%$ ) the storage modulus is proportional to the square of concentration.<sup>50</sup>

<sup>a</sup>Address for correspondence: Thayer School of Engineering, Dartmouth College, Hanover, New Hampshire 03755. Telephone: (603) 646-0775; fax: (603) 646-3856; electronic mail: Marvin.M.Doyley@Dartmouth.edu

<sup>1</sup>M. Tristram, D. C. Barbosa, D. O. Cosgrove, D. K. Nassiri, J. C. Bamber, and C. R. Hill, "Ultrasonic study of in vivo kinetic characteristics of human tissues," *Ultrasound Med. Biol.* **12**, 927–937 (1986).

<sup>2</sup>T. A. Krouskop, T. M. Wheeler, F. Kallel, B. S. Garra, and T. Hall, "Elastic moduli of breast and prostate tissues under compression," *Ultrason. Imaging* **20**, 260–274 (1998).

<sup>3</sup>A. P. Savazyn, A. Skovoroda, and D. Vucelic, "Elasticity imaging as a new modality of medical imaging for cancer detection," *Premieres Journees D'etudes*, 1994.

<sup>4</sup>J. Ophir, I. Cespedes, H. Ponnekanti, Y. Yazdi, and X. Li, "Elastography: A quantitative method for imaging the elasticity of biological tissues," *Ultrason. Imaging* **13**, 111–134 (1991).

<sup>5</sup>M. O'Donnell, A. R. Skovoroda, and B. M. Shapo, "Measurement of arterial wall motion using Fourier based speckle tracking algorithm," in *IEEE Ultrasonics Symposium*, Orlando, FL, 1991.

<sup>6</sup>K. J. Parker, S. R. Huang, R. A. Musulin, and R. M. Lerner, "Tissue response to mechanical vibrations for 'sonoelasticity imaging,'" *Ultrasound Med. Biol.* **16**, 241–246 (1990).

<sup>7</sup>J. C. Bamber and N. L. Bush, *Freehand Elasticity Imaging Using Speckle*

*Decorrelation Rate*, edited by P. Totoli and L. Masotti (Plenum, New York, 1995), Vol. 22, pp. 285–292.

<sup>8</sup>T. A. Krouskop, D. R. Dougherty, and F. S. Vinson, "A pulsed Doppler ultrasonic system for making noninvasive measurements of the mechanical properties of soft tissue," *J. Rehabil. Res. Dev.* **24**, 1–8 (1987).

<sup>9</sup>J. Ophir, S. K. Alam, B. Garra, F. Kallel, E. Konofagou, T. Krouskop, and T. Varghese, "Elastography: ultrasonic estimation and imaging of the elastic properties of tissues," *Proc. Inst. Mech. Eng. Part H, J. Eng. Med.* **213**, 203–233 (1999).

<sup>10</sup>L. Gao, K. J. Parker, R. M. Lerner, and S. F. Levinson, "Imaging of the elastic properties of tissue—a review," *Ultrasound Med. Biol.* **22**, 959–977 (1996).

<sup>11</sup>K. J. Parker, L. Gao, R. M. Lerner, and S. F. Levinson, "Techniques for elasticity imaging: A review," *IEEE Eng. Med. Biol. Mag.* 52–59 (1996).

<sup>12</sup>J. C. Bamber, P. E. Barbone, N. L. Bush, D. O. Cosgrove, M. M. Doyley, F. G. Fuchsel, P. M. Meaney, N. R. Miller, T. Shiina, and F. Tranquart, "Progress in freehand elastography of the breast," *IEICE Trans. Inf. Syst.* **E85D**, 5–14 (2002).

<sup>13</sup>B. S. Garra, E. I. Cespedes, J. Ophir, S. R. Spratt, R. A. Zuurbier, C. M. Magnant, and M. F. Pennanen, "Elastography of breast lesions: Initial clinical results," *Radiology* **202**, 79–86 (1997).

<sup>14</sup>D. J. Rubens, M. A. Hadley, S. K. Alam, L. Gao, R. D. Mayer, and K. J. Parker, "Sonoelasticity imaging of prostate cancer: *In vitro* results," *Radiology* **195**, 379–383 (1995).

<sup>15</sup>F. G. Fuchsel, N. L. Bush, F. Tranquart, J. C. Bamber, D. O. Cosgrove, and N. R. Miller, "Ultrasound freehand elastography: Evaluation of diagnostic potential in clinical breast imaging," *Radiology* **221**, 188 (2001).

<sup>16</sup>K. M. Hiltawsky, M. Kruger, C. Starke, L. Heuser, H. Ermer, and A. Jensen, "Freehand ultrasound elastography of breast lesions: Clinical results," *Ultrasound Med. Biol.* **27**, 1461–1469 (2001).

<sup>17</sup>T. L. Chenevert, A. R. Skovoroda, M. O'Donnell, and S. Y. Emelianov, "Elasticity reconstructive imaging by means of stimulated echo MRI," *Magn. Reson. Med.* **39**, 482–490 (1998).

<sup>18</sup>D. D. Steele, T. L. Chenevert, A. R. Skovoroda, and S. Y. Emelianov, "Three-dimensional static displacement, stimulated echo NMR elasticity imaging," *Phys. Med. Biol.* **45**, 1633–1648 (2000).

<sup>19</sup>J. B. Fowlkes, S. Y. Emelianov, J. G. Pipe, A. R. Skovoroda, P. L. Carson, R. S. Adler, and A. P. Sarvazyan, "Magnetic-resonance imaging techniques for detection of elasticity variation," *Med. Phys.* **22**, 1771–1778 (1995).

<sup>20</sup>J. Bishop, A. Samani, J. Sciarretta, and D. B. Plewes, "Two-dimensional MR elastography with linear inversion reconstruction: Methodology and noise analysis," *Phys. Med. Biol.* **45**, 2081–2091 (2000).

<sup>21</sup>J. Bishop, A. Samani, J. Sciarretta, C. Luginbuhl, and D. B. Plewes, "A signal/noise analysis of quasi-static MR elastography," *IEEE Trans. Med. Imaging* **20**, 1183–1187 (2001).

<sup>22</sup>D. B. Plewes, S. Silver, B. Starkoski, and C. L. Walker, "Magnetic resonance imaging of ultrasound fields: Gradient characteristics," *J. Magn. Reson. Imaging* **11**, 452–457 (2000).

<sup>23</sup>D. B. Plewes, J. Bishop, A. Samani, and J. Sciarretta, "Visualization and quantification of breast cancer biomechanical properties with magnetic resonance elastography," *Phys. Med. Biol.* **45**, 1591–1610 (2000).

<sup>24</sup>D. B. Plewes, I. Betty, S. N. Urchuk, and I. Soutar, "Visualizing tissue compliance with MR imaging," *J. Magn. Reson. Imaging* **5**, 733–738 (1995).

<sup>25</sup>R. Muthupillai, D. J. Lomas, P. J. Rossman, J. F. Greenleaf, A. Manduca, and R. L. Ehman, "Magnetic resonance elastography by direct visualization of propagating acoustic strain waves," *Science* **269**, 1854–1857 (1995).

<sup>26</sup>R. Muthupillai and R. L. Ehman, "Magnetic resonance elastography," *Nat. Med.* **2**, 601–603 (1996).

<sup>27</sup>R. Sinkus, J. Lorenzen, D. Schrader, M. Lorenzen, M. Dargatz, and D. Holz, "High-resolution tensor MR elastography for breast tumour detection," *Phys. Med. Biol.* **45**, 1649–1664 (2000).

<sup>28</sup>J. B. Weaver, E. E. Van Houten, M. I. Miga, F. E. Kennedy, and K. D. Paulsen, "Magnetic resonance elastography using 3D gradient echo measurements of steady-state motion," *Med. Phys.* **28**, 1620–1628 (2001).

<sup>29</sup>E. E. Van Houten, K. D. Paulsen, M. I. Miga, F. E. Kennedy, and J. B. Weaver, "An overlapping subzone technique for MR-based elastic property reconstruction," *Magn. Reson. Med.* **42**, 779–786 (1999).

<sup>30</sup>E. E. Van Houten, M. I. Miga, J. B. Weaver, F. E. Kennedy, and K. D.

- Paulsen, "Three-dimensional subzone-based reconstruction algorithm for MR elastography," *Magn. Reson. Med.* **45**, 827–837 (2001).
- <sup>31</sup> B. W. Pogue, C. Wilscher, T. O. McBride, U. L. Osterberg, and K. D. Paulsen, "Contrast-detail analysis for detection and reconstruction with near-infrared diffuse tomography," *Med. Phys.* **27**, 2693–2699 (2000).
- <sup>32</sup> H. Lopez, M. Loew, P. Butler, M. Hill, and R. Allman, "A clinical evaluation of contrast-detail analysis for ultrasound images," *Med. Phys.* **17**, 48–57 (1990).
- <sup>33</sup> T. Hall, M. Insana, N. M. Soller, and L. Harrison, "Ultrasound contrast-detail analysis: a preliminary study in human observer performance," *Med. Phys.* **20**, 117–127 (1993).
- <sup>34</sup> R. Wagner and D. Brown, "Unified SNR analysis of medical imaging systems," *Phys. Med. Biol.* **30**, 489–518 (1985).
- <sup>35</sup> K. J. Robinson, C. J. Kotre, and K. Faulkner, "The use of contrast-detail test objects in the optimization of optical density in mammography," *Br. J. Radiol.* **68**, 277–282 (1995).
- <sup>36</sup> N. R. Miller and J. C. Bamber, "Thresholds for visual detection of Young's modulus contrast in simulated ultrasound image movies," *Phys. Med. Biol.* **45**, 2057–2059 (2000).
- <sup>37</sup> H. Lopez, M. H. Loew, and D. J. Goodenough, "Objective analysis of ultrasound images by use of a computational observer," *IEEE Trans. Med. Imaging* **11**, 496–506 (1992).
- <sup>38</sup> J. J. Rownd, E. L. Madsen, and J. A. Zagzebski, "Phantoms and automated systems for testing the resolution of ultrasound scanners," *Ultrasound Med. Biol.* **23**, 245–260 (1997).
- <sup>39</sup> C. L. de Korte, E. I. Cespedes, A. F. van der Steen, B. Norder, and K. te Nijenhuis, "Elastic and acoustic properties of vessel mimicking material for elasticity imaging," *Ultrason. Imaging* **19**, 112–126 (1997).
- <sup>40</sup> K. D. Paulsen, X. Jia, and J. M. Sullivan, "Finite element computations of specific absorption rates in anatomically-conforming full-body models for hyperthermia treatment analysis," *IEEE Trans. Biomed. Eng.* **40**, 933–945 (1993).
- <sup>41</sup> W. E. Lorensen and H. Cline, "Marching Cube: A high resolution 3D surface construction algorithm," *Comput. Graphics* **21** (1987).
- <sup>42</sup> F. Kallel and M. Bertrand, "Tissue elasticity reconstruction using linear perturbation method," *IEEE Trans. Med. Imaging* **15**, 299–313 (1996).
- <sup>43</sup> D. W. Marquardt, "An algorithm for least-squares estimation of nonlinear parameters," *J. Soc. Ind. Appl. Math.* 431–441 (1963).
- <sup>44</sup> M. M. Doyley, P. M. Meaney, and J. C. Bamber, "Evaluation of an iterative reconstruction method for quantitative elastography," *Phys. Med. Biol.* **45**, 1521–1540 (2000).
- <sup>45</sup> P. Chaturvedi, M. F. Insana, and T. J. Hall, "2-D companding for noise reduction in strain imaging," *IEEE Trans. Ultrason. Ferroelectr. Freq. Control* **45**, 179–191 (1998).
- <sup>46</sup> M. Bilgen, "Target detectability in acoustic elastography," *IEEE Trans. Ultrason. Ferroelectr. Freq. Control* **46**, 1128–1133 (1997).
- <sup>47</sup> N. R. Miller and J. C. Bamber, "Thresholds for visual detection of Young's modulus contrast in simulated ultrasound image movies," *Phys. Med. Biol.* **45**, 2057–2079 (2000).
- <sup>48</sup> H. Schott, "Kinetics of swelling of polymers and their gels," *J. Pharm. Sci.* **81**, 467–470 (1992).
- <sup>49</sup> F. Kallel, C. D. Prihoda, and J. Ophir, "Contrast-transfer efficiency for continuously varying tissue moduli: simulation and phantom validation," *Ultrasound Med. Biol.* **27**, 1115–1125 (2001).
- <sup>50</sup> A. G. Ward, R. Frederick, E. Eirich, and P. R. Saunders, *Rheology: Theory and Applications* (Academic, New York, 1958).

# INTRODUCING PlanCHECK™

The newly-integrated first phase in  
the SunCHECK™ Patient workflow

Streamline **plan  
quality verification**  
with comprehensive,  
automated Physics and  
Dosimetric Checks.

Learn More 

